

Kinematics-Aware Multi-Policy Reinforcement Learning for Force-Capable Humanoid Loco-Manipulation

Kaiyan Xiao^{1,†}, Zihan Xu^{1,†}, Cheng Zhe¹, Chengju Liu^{1,2}, Qijun Chen^{1,2}

Abstract—Humanoid robots, with their human-like morphology, hold great potential for industrial applications. However, existing loco-manipulation methods primarily focus on dexterous manipulation, falling short of the combined requirements for dexterity and proactive force interaction in high-load industrial scenarios. To bridge this gap, we propose a reinforcement learning-based framework with a decoupled three-stage training pipeline, consisting of an upper-body policy, a lower-body policy, and a delta-command policy. To accelerate upper-body training, a heuristic reward function is designed. By implicitly embedding forward kinematics priors, it enables the policy to converge faster and achieve superior performance. For the lower body, a force-based curriculum learning strategy is developed, enabling the robot to actively exert and regulate interaction forces with the environment. To ensure robust whole-body coordination, a delta-command policy is employed to counteract vertical end-effector displacements in the world frame resulting from lower-body motion. Extensive simulation and real-world experiments on the Unitree G1 humanoid robot validate the proposed framework, showcasing its capability to accomplish high-payload tasks such as walking while carrying a 4 kg object and pushing or pulling a cart with a total load of 112.8 kg.

Index Terms—Humanoid robot loco-manipulation, reinforcement learning, multi-policy, force-capable.

I. INTRODUCTION

HUMANOID robots are increasingly considered for deployment in industrial settings, where various tools and workflows are originally designed for human operators. As large-scale customization is often impractical, humanoid robots, owing to their morphology and natural operational compatibility, can seamlessly interface with and utilize existing tools.

While humanoid robots have demonstrated considerable dexterous manipulation capabilities in low-load scenarios, such as tidying objects [1], delivery [2], and cleaning [3], reliance on dexterity alone is insufficient when extending to labor-intensive industrial applications. In high-load automated production environments, common tasks include bimanual handling of heavy components [4], supporting or operating large-scale tools [5], and transporting materials using carts [6]. These tasks typically require robots to possess both locomotion

and manipulation capabilities, representing a canonical loco-manipulation problem. However, unlike low-load manipulation tasks where precise motion dominates, high-load scenarios introduce significant dynamic coupling between the upper-body force exertion and lower-body stability, making whole-body coordination substantially more challenging.

Reinforcement learning (RL) has recently demonstrated strong potential for whole-body motion control in humanoid robots, enabling stable locomotion across diverse terrains [7] as well as highly expressive, human-like behaviors through the use of motion capture (MoCap) data [8]. Whole-body RL-based motion control can be broadly categorized into two approaches: monolithic whole-body control [9], [10] and decoupled modular control [2], [11], [12]. Although monolithic whole-body control can theoretically generate natural and coordinated motions, it often struggles to simultaneously address both locomotion and manipulation tasks in high degree of freedom (DoF) humanoid robots, resulting in low training efficiency and insufficient exploration [2]. Some works mitigate this issue by leveraging MoCap data to guide policy learning [13]–[15]. However, MoCap data inherently lack information about the force interactions between the robot and the environment, which limits the policy’s ability to learn interaction-rich behaviors.

By separating the robot into upper- and lower-body modules, decoupled controllers alleviate the challenges associated with high-dimensional optimization [11]. Despite this advantage, several critical limitations remain. The upper-body typically relies on inverse kinematics for end-effector pose tracking [2], [12], which becomes computationally intensive for high-DoF manipulators and struggles to meet real-time requirements [16]. Its incompatibility with reinforcement learning frameworks further constrains the upper-body’s generalization capability in industrial settings. Meanwhile, existing lower-body methods primarily focus on passive adaptation to external disturbances to ensure stable locomotion [2], [11]. The ability to actively exert forces on the environment, which is a key requirement for high-load industrial tasks, has received little attention. Furthermore, achieving effective coordination between the upper- and lower-body modules within a decoupled framework remains largely unresolved [17]. Collectively, these challenges highlight a critical gap in enabling humanoid robots to perform robust, high-load tasks in complex industrial scenarios.

[†] equal contribution

¹ the Robot and Artificial Intelligence Lab, College of Electronic and Information Engineering, Tongji University, Shanghai 201804, China

² State Key Laboratory of Autonomous Intelligent Unmanned Systems (Tongji University), Shanghai, China
{xiaokaiyan, xuzihan}@tongji.edu.cn

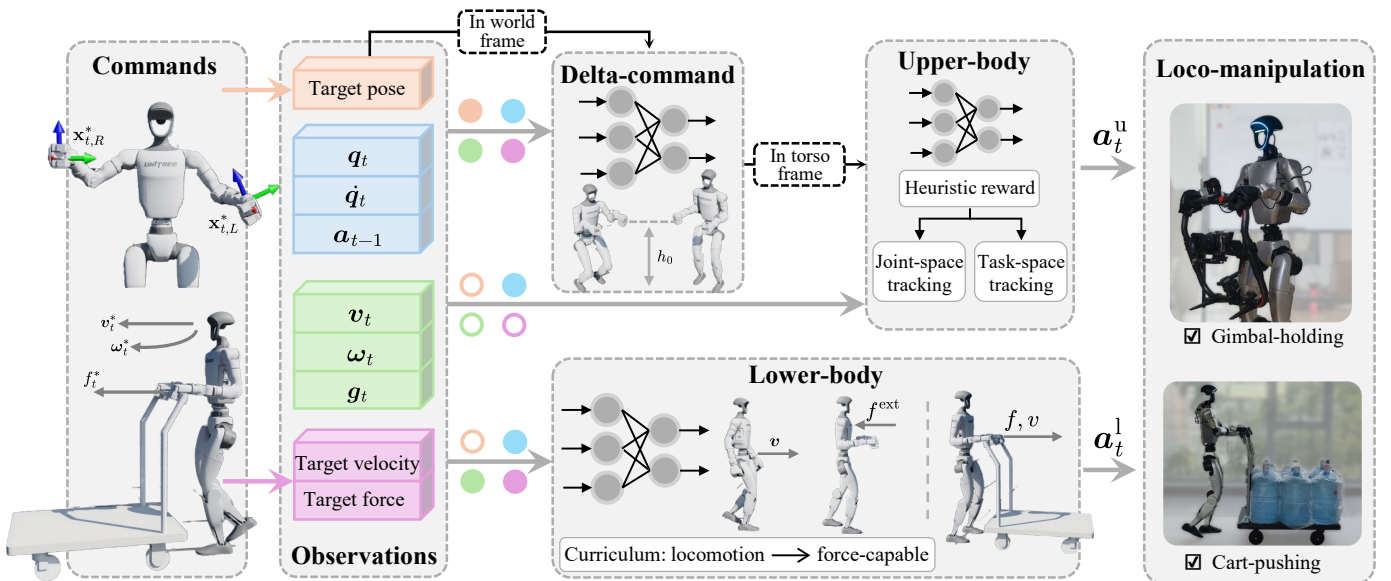


Fig. 1. System architecture of the proposed training pipeline. The diagram illustrates the integration of the upper-body policy, lower-body policy, and delta-command policy for coordinated loco-manipulation tasks. When observation data are propagated, filled circles indicate the output of data in the corresponding color, whereas hollow circles indicate data not output.

To address the aforementioned challenges, this work proposes a RL-based humanoid loco-manipulation framework, as illustrated in Fig. 1. The framework employs a three-stage training pipeline to endow humanoid robots with capabilities suitable for industrial applications. It operates within a command space defined by end-effector poses, locomotion velocity, and target exerted force, together with corresponding robot states as observations. A key component of the framework is the delta-command module, which computes a compensatory offset for the end-effector pose in the torso frame. This offset mitigates vertical disturbances caused by torso motion during locomotion. The compensated pose serves as a reference for the upper-body policy, while the lower-body policy generates locomotion actions, together achieving coordinated whole-body control. Besides, during upper-body training, a heuristic reward function combining joint-angle errors and end-effector pose errors is designed. By implicitly embedding forward kinematics priors, the policy learns the mapping between joint configurations and end-effector poses rapidly. Moreover, in the lower-body training stage, we adopt a curriculum learning strategy to sequentially endow the policy with locomotion and force-capable skills. After the policy masters basic locomotion, target exerted forces are introduced, and external disturbances of equal magnitude but opposite direction to the target exerted force are applied to the robot in simulation. The policy is then trained to maintain stable locomotion under these conditions, gradually acquiring the ability to exert forces proactively.

The main contributions of this work are summarized as follows:

- 1) To enhance both training efficiency and performance of the upper-body, a heuristic reward function is designed, achieved by implicitly embedding forward kinematics priors.
- 2) A force-based curriculum learning approach is proposed

to endow the robot with force-capable skills, enhancing its adaptability in high-load and strong-interaction tasks.

- 3) By introducing a delta-command policy, motion coordination under decoupled upper- and lower-body control is achieved.
- 4) A three-stage RL framework for industrial loco-manipulation is proposed. By coordinating three-modular policies, the Unitree G1 robot achieves stable locomotion while carrying a 4 kg object and pushing or pulling a cart with a load of 112.8 kg.

The remainder of this paper is organized as follows. Section II reviews the related literature. Section III introduces the proposed three-stage training pipeline. Section IV presents simulation and hardware experiments conducted to validate the effectiveness of the framework. Finally, Section V concludes the paper.

II. RELATED WORKS

A. Model-based Approaches for Loco-manipulation

Model-based loco-manipulation controllers have a long history, typically framing loco-manipulation as an optimal control problem [18]–[20]. Prior work has explored various strategies to enhance performance. Karim et al. [21] unify task-space multi-objective controllers into a quadratic program, enabling physically consistent position and force control across manipulation tasks. Murooka et al. [22] propose a frequency-domain stabilization method that explicitly accounts for external forces, adjusting the center of mass and zero moment point to track force references. Li et al. [23] develop a model predictive control framework based on a simplified rigid body model, demonstrating dynamic locomotion and manipulation on uneven terrain. Other works explore decomposition of locomotion and manipulation into action primitives [24] or adapt contact locations based on measured forces [25].

Despite these advances, applying model-based controllers in real-world scenarios remains challenging. They rely on accurate system dynamics and environment models, making them sensitive to modeling errors and unpredictable variations in contact forces, payloads, friction, and sensor noise. As a result, their robust performance is often compromised outside controlled settings, limiting practical deployment in complex industrial environments.

B. RL for Humanoid Locomotion

Model-based methods are theoretically capable of generating stable gaits, yet their real-world application is hindered by poor adaptation to complex terrains and external disturbances. As a result, reinforcement learning (RL) has emerged as a more promising paradigm for tackling the challenges of humanoid locomotion control. Lee et al. [26] established the fundamental principles of generating stable gaits for legged robots through reinforcement learning. Building upon this foundation, subsequent works introduced domain randomization to enable sim-to-real transfer of RL policies [27], achieving robust performance on physical humanoid robots [28]. Meanwhile, the emergence of large-scale parallel simulation platforms such as IsaacSim [29] and MuJoCo [30] has made large-scale RL training feasible, further advancing RL-based progress and breakthroughs in robotic locomotion control. In recent years, RL-powered humanoid robots have not only maintained stable locomotion under diverse terrains and external perturbations, but have also demonstrated the capability to perform more complex skills, such as jumping [31], stair climbing [32], and even parkour [33].

These advances collectively indicate that RL-based humanoid locomotion control has matured significantly, demonstrating robustness, reproducibility, and real-world deployability across diverse conditions. This maturity establishes a solid foundation upon which integrated loco-manipulation frameworks, proposed in this paper, can effectively build.

C. RL-based Whole-Body Control for Loco-manipulation

With the advancement of RL-based locomotion methods, RL has also been applied to the training of whole-body controllers for humanoid [34]–[37]. These controllers are typically categorized into monolithic control and decoupled modular control. Monolithic control often relies on motion-capture data as reference trajectories. AMP [38] incorporates expert priors and employs adversarial learning to generate natural motions. H2O [13], on the other hand, leverages large-scale motion-capture datasets to enable dexterous manipulation. Ze et al. [39] present a teleoperation system that combines RL and behavior cloning to achieve real-time, coordinated whole-body control. Nevertheless, such approaches are limited to motion imitation and fail to learn active force interactions with the environment.

In decoupled control frameworks, Ben et al. [2] employ inverse kinematics and PD controllers for upper-body control, while utilizing a RL policy for lower-body locomotion, and further design an isomorphic exoskeleton to facilitate intuitive teleoperation by human operators. Lu et al. [12] adopt a

similar modular architecture and introduce PMP, a learned latent representation of upper-body motion, to condition the lower-body RL policy, thereby ensuring dynamic stability and coordination in whole-body tasks. While these approaches leverage inverse kinematics to achieve dexterous upper-body manipulation, their reliance on kinematic control inherently limits force generation and adaptability, rendering them unsuitable for high-load industrial scenarios. The study [11] further incorporates force interactions through a force curriculum that jointly trains upper- and lower-body policies, equipping the robot with force-adaptive capabilities. Nevertheless, the interaction remains reactive rather than proactive, limiting the robot’s ability to actively exert and regulate forces in dynamic environments.

D. Our Approach

The proposed loco-manipulation framework draws inspiration from several previous studies. For upper-body training, the study by Xu et al. [40] employs a joint angle signal network to map joint angles to end-effector poses. We extend this approach from offline to online training and further adopt the bilevel optimization strategy from Xie et al. [41] to tune the parameters of heuristic reward functions during training. For lower-body training, we build upon the training pipeline of the study [32] and extend the force-adaptive approach presented by Zhang et al. [11], which applies forces at the robot’s end-effectors to enable adaptive interaction. During our training pipeline, force commands are introduced and reaction forces corresponding to the target exerted force are applied to the robot’s torso, equipping the robot with the ability to actively exert forces on the environment during real-world deployment. Finally, while the work of He et al. [8] introduces a delta-action module to reduce the simulation-to-reality gap, we propose a delta-command module to address discrepancies between task-space and operational-space commands.

III. APPROACH

As illustrated in Fig. 1, the proposed framework consists of three policies. Section III-A defines the problem, Section III-B presents the upper-body policy, Section III-C describes the lower-body policy, and Section III-D introduces the delta-command policy.

A. Problem Formulation

The Unitree G1 humanoid robot is adopted as the experimental platform, which features a total of $n = 29$ actuated joints. The DoFs are partitioned into $n^l = 15$ lower-body joints (waist, hip, knee, ankle) and $n^u = 14$ upper-body joints (shoulder, elbow, wrist).

We formulate the humanoid loco-manipulation problem as a goal-conditioned RL task. The problem is defined by a Markov Decision Process (MDP):

$$\mathcal{M} = (\mathcal{S}, \mathcal{A}, \mathcal{G}, \mathcal{P}, \mathcal{R}, \gamma), \quad (1)$$

where \mathcal{S} is the state space of the humanoid robot, \mathcal{A} is the robot’s action space, \mathcal{G} is the goal space, \mathcal{P} is the state

Algorithm 1: Sampling End-effector Poses

Input: Left end-effector’s task-space \mathcal{W}_L , left arm joints’ upper and lower limits $q_L^{u,\max}$, $q_L^{u,\min}$

Output: q^{u*} , $x_L^{\text{torso}*}$, $x_R^{\text{torso}*}$

```

1 repeat
2    $u \leftarrow (u_0, \dots, u_{\frac{n}{2}})$ ,  $u_i \sim \mathcal{U}(0, 1)$ 
3    $q_L^{u*} \leftarrow q_L^{u,\min} + u \odot (q_L^{u,\max} - q_L^{u,\min})$ 
4    $x_L^{\text{torso}*} \leftarrow \text{FK}(q_L^{u*})$  // FK( $\cdot$ ) represents
   forward kinematic computation.
5   Compute left end-effector’s direction vector  $e_L$ 
6   Compute left elbow link’s direction vector  $e_{\text{elbow}}$ 
7    $\vartheta \leftarrow \cos^{-1}\left(\frac{e_L \cdot e_{\text{elbow}}}{\|e_L\| \|e_{\text{elbow}}\|}\right)$ 
8 until  $x_L^{\text{torso}*} \in \mathcal{W}_L$  and  $\vartheta < \frac{\pi}{2}$ 
9  $q_R^{u*} \leftarrow \text{Mir}(q_L^{u*})$  // Mir( $\cdot$ ) mirrors left joint
   angles to right arm.
10  $x_R^{\text{torso}*} \leftarrow \text{FK}(q_R^{u*})$ 
11  $q^{u*} \leftarrow [q_L^{u*}, q_R^{u*}]$ 
12 return  $q^{u*}$ ,  $x_L^{\text{torso}*}$ ,  $x_R^{\text{torso}*}$ 
    
```

transition probability function, \mathcal{R} is the reward function and $\gamma \in [0, 1)$ is the discount factor.

At each time step t , upper-body proprioception s_t^u and lower-body proprioception s_t^l are aggregated into the robot’s overall proprioception state $s_t \in \mathcal{S}$.

$$\begin{aligned} s_t^u &= [q_t^u, \dot{q}_t^u, a_{t-1}^u], \\ s_t^l &= [q_t^l, \dot{q}_t^l, \omega_t, g_t, a_{t-1}^l], \\ s_t &= [q_t, \dot{q}_t, \omega_t, g_t, a_{t-1}], \end{aligned} \quad (2)$$

where $q_t \in \mathbb{R}^n$ and $\dot{q}_t \in \mathbb{R}^n$ are the joint positions and velocities, $\omega_t \in \mathbb{R}^3$ is the root angular velocity, $g_t \in \mathbb{R}^3$ is the projected gravity, and $a_{t-1} \in \mathbb{R}^n$ is the action in the last time step.

The goal space \mathcal{G}_t consists of manipulation goals \mathcal{G}_t^u , locomotion goals \mathcal{G}_t^l , and high-level coordination goals \mathcal{G}_t^h .

$$\begin{aligned} \mathcal{G}_t^u &= \{x_{t,i}^{\text{torso}*}\}_{i \in \{L,R\}}, \\ \mathcal{G}_t^l &= [v_t^*, \omega_t^*, f_t^*], \\ \mathcal{G}_t^h &= \{x_{t,i}^{\text{world}*}\}_{i \in \{L,R\}}. \end{aligned} \quad (3)$$

Let the subscripts “L” and “R” denotes the left and right end-effectors of the upper-body, x^j is defined as the end-effector’s pose relative to the j -frame, represented in Cartesian coordinates and Euler angles. v_t , ω_t and f_t represent root linear velocity, root angular velocity, and the magnitude of forces applied to the environment, respectively. Throughout this paper, the superscript “*” is used to indicate the target (or commanded) state of the robot.

In the framework depicted in Fig. 1, the goal space (commands) include the upper-body end-effector poses in the world coordinate frame, locomotion velocity, and target exerted force. Together with the robot’s states, these commands constitute the observation space, where filled circles indicate the inclusion of the corresponding observations and hollow circles indicate their absence. Based on these definitions, our approach decouples the whole-body control problem into three

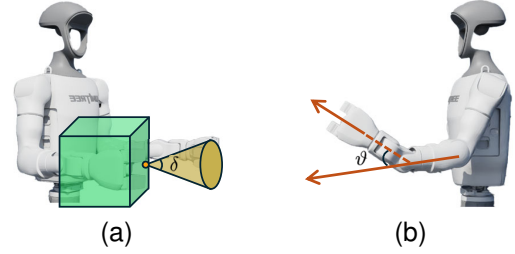


Fig. 2. Task-Space and Imposed Constraints of the Upper Body. (a) Task-space of the upper body. The Task-spaces of the left and right end-effectors are symmetric with respect to the x -axis of the torso frame. The green cuboid illustrates the set of feasible positions, whereas the yellow cone indicates the feasible orientation range of the end-effector, with the aperture angle δ defining the orientation limits. (b) Illustration of the angle between the elbow link’s direction and the end-effector’s direction.

separate policies. The high-level delta-command policy π^h does not directly participate in robot control. The basic upper-body agent learns a policy $\pi^u: s_t^u \times \mathcal{G}_t^u \mapsto a_t^u$, while the lower-body agent learns a policy $\pi^l: s_t^l \times \mathcal{G}_t^l \mapsto a_t^l$. Each policy is optimized to maximize the expected cumulative reward:

$$\max_{\theta_i} \mathbb{E}\left[\sum_{t=1}^T \gamma_{t-1} \cdot r_t^i\right], \quad r_t^i = \mathcal{R}^i(s_t^i, \mathcal{G}_t^i), \quad i \in \{u, l, h\}, \quad (4)$$

where θ_i denotes the parameters of the policy i , and T is the episode length. r_t^i is the scalar reward at timestep t , computed from the agent’s current state s_t^i and its task goal \mathcal{G}_t^i through the reward function $\mathcal{R}^i(\cdot)$. γ is the discount factor that balances immediate and future rewards.

During execution, the combined action a_t from upper- and lower-body policies is directly mapped to the desired joint positions q_t^{des} :

$$\begin{aligned} a_t &= [\lambda^u a_t^u, \lambda^l a_t^l], \\ q_t^{\text{des}} &= a_t + q^{\text{default}}. \end{aligned} \quad (5)$$

Where λ^u and λ^l are the action scaling factor for upper- and lower-body, q^{default} represents the default joint positions. q_t^{des} is then tracked by a joint-level PD controller, with the resulting motor torques τ_t computed as:

$$\tau_t = K_p(q_t^{\text{des}} - q_t) - K_d \cdot \dot{q}_t, \quad (6)$$

where K_p and K_p are diagonal gain matrices of stiffness and damping.

B. Heuristic Upper-body Policy Optimization

Precise control of the upper-body is a prerequisite for humanoid robots to perform loco-manipulation tasks. The Unitree G1 robot is equipped with two 7-DoF arms, providing a large workspace. Direct applying RL over such a continuous and high-dimensional workspace often results in inefficient data collection and slow policy convergence. To address this issue, a heuristic method that leverages kinematic priors to guide policy convergence is designed.

The training pipeline of the upper-body policy is presented as follows. End-effector poses are sampled using Alg. 1. In the

sampling process, the poses are filtered to improve data quality and prevent non-physical postures. Specifically, the end-effector position must lie within the predefined task-space (as shown in Fig. 2(a)), and the angle between the homogeneous elbow link direction and the end-effector direction must be less than 90° (as shown in Fig. 2(b)). Furthermore, a mirror trick is applied to prevent performance inconsistency between the left and right hands caused by random sampling.

Based on the sampling method, the heuristic reward function R^u , which implicitly encodes kinematic information, is formulated as:

$$R^u = \alpha^{\text{joint}} \cdot r^{\text{joint}} + \alpha^{\text{pose}} \cdot r^{\text{pose}}. \quad (7)$$

To simultaneously track the objective pose in both the joint-space and the task-space, R^u is decomposed into two terms, where α^{joint} and α^{pose} are weighting factors balancing their respective contributions. The joint-space term measures the discrepancy between the current joint position and the target joint positions, as expressed below:

$$r^{\text{joint}} = \exp\left(-\frac{\|\mathbf{q}^u - \mathbf{q}^{u*}\|}{\sigma^2}\right), \quad (8)$$

where σ is a scaling parameter that controls the sensitivity of the joint-space exponential term. In contrast, the task-space term is formulated to directly capture the difference between the current end-effector pose and the target pose, as shown in the following equation:

$$\begin{aligned} \Delta\phi &= \sum_{i \in \{L,R\}} \|\text{Log}(\eta_i^{\text{torso}} \otimes \hat{\eta}_i^{\text{torso}*})\|, \\ r^{\text{pose}} &= \|\mathbf{d}_i^{\text{torso}*} - \mathbf{d}_i^{\text{torso}}\|_{i \in \{L,R\}} + \frac{1}{2}\Delta\phi, \end{aligned} \quad (9)$$

Where η^j denote the orientation of the end-effector in j -frame as quaternion form, $\hat{\eta}$ is the conjugate of the quaternion, the operator \otimes denotes the quaternion multiplication, $\text{Log}(\cdot)$ converts a quaternion into axis-angle representation, \mathbf{d}^k represents the end-effector's position in k -frame, and $\Delta\phi$ is the orientation error.

In the context of the heuristic reward function, the weighting factors α^{joint} and α^{pose} , as well as the scale parameter σ , are dynamically adjusted to guide the learning process. In the early stage, a higher weight is assigned to the joint-space term r^{joint} , allowing the forward kinematic information embedded in the reward function to guide the agent efficiently toward the vicinity of the target poses. As σ gradually decreases, the robot's joint tracking error is further reduced, which facilitates rapid convergence by reducing inefficient exploration in the sparse-reward task-space. As the policy begins to converge, the weight of the task-space term r^{pose} is increased, encouraging the agent to refine its end-effector trajectories and achieve precise task-space tracking.

C. Force-capable Lower Body Curriculum Learning

Lower-body policy primarily governs the robot's locomotion capability. The proposed lower-body training pipeline diverges from existing methods by integrating force-capable training,

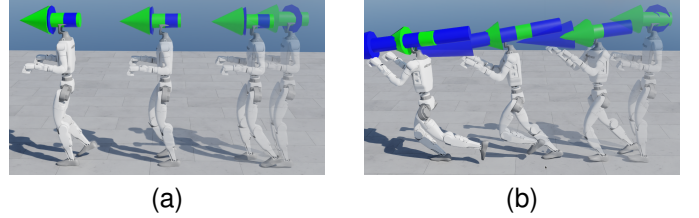


Fig. 3. Comparison of training outcomes with and without the sampling strategy. Both (a) and (b) are trained using curriculum learning, but only (a) incorporates the sampling strategy. Green arrows denote target velocities, and blue arrows denote actual velocities. The target linear velocity is set to $v_t^* = 0.7$ m/s, while the target force is $f_t^* = 0$ N. Without the sampling strategy, the policy tends to converge toward high-force scenarios, resulting in degraded locomotion performance under low-force conditions. In contrast, the agent trained with the sampling strategy exhibits improved generalization to varying force levels.

which enables the robot to actively apply forces to the environment and thereby significantly enhancing its interaction capabilities.

To achieve the force-capable training objective, an additional force target f_t^* is introduced in the lower-body goal space \mathcal{G}_t^l . The direction of f_t^* is set opposite to the robot's linear velocity, while its magnitude is sampled from a dynamic range according to a designed procedure. Once f_t^* is determined, the simulation environment applies an equal and opposite force to the robot's torso in accordance with Newton's third law, which is necessary to make the training effective. However, continuously applying external forces during locomotion training presents a significant challenge. If the target force f_t^* exceeds the agent's locomotion capability, it can hinder or slow down convergence. To address this, curriculum learning is incorporated into the lower-body training, enabling the agent to sequentially acquire locomotion and force-capable skills.

During the training of the lower-body policy, the force magnitude f_t^* is sampled according to:

$$f_t^* = \begin{cases} 0, & \text{if } u \leq 0.1, \\ \mathcal{U}(0, f_t^{\text{max}}), & \text{if } 0.1 < u \leq 0.5, u \sim \mathcal{U}(0, 1) \\ f_t^{\text{max}}, & \text{if } u > 0.5, \end{cases} \quad (10)$$

where f_t^{max} denotes the upper bound of the force at the current time step. Furthermore, the progression of the force curriculum is regulated by multiple evaluation metrics, which are summarized as follows:

$$\mathcal{C} = \mathcal{C}_{\text{lin}} \wedge \mathcal{C}_{\text{ang}} \wedge \mathcal{C}_{\text{dis}} \wedge \mathcal{C}_{\text{force}} \quad (11)$$

where each metric is defined as follows:

$$\begin{aligned} \mathcal{C}_{\text{lin}} &= \frac{1}{N_{\text{steps}}} \sum_{i=1}^{N_{\text{steps}}} \|\mathbf{v}_i^* - \mathbf{v}_i\| < \varepsilon_{\text{lin}}, \\ \mathcal{C}_{\text{ang}} &= \frac{1}{N_{\text{steps}}} \sum_{i=1}^{N_{\text{steps}}} \|\boldsymbol{\omega}_i^* - \boldsymbol{\omega}_i\| < \varepsilon_{\text{ang}}, \\ \mathcal{C}_{\text{dis}} &= \|p_o^{xy} - p^{xy}\| > \varepsilon_{\text{dis}}, \\ \mathcal{C}_{\text{force}} &= \begin{cases} 1, & \text{if } f_t^* = f_t^{\text{max}}, \\ 0, & \text{otherwise.} \end{cases} \end{aligned} \quad (12)$$

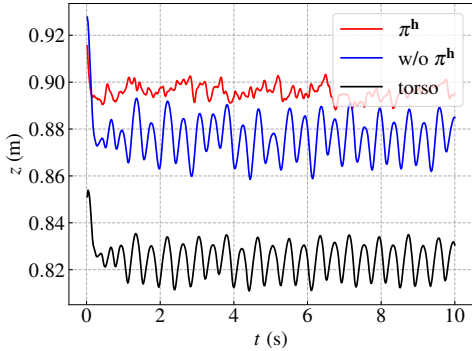


Fig. 4. Comparison of end-effector height trajectories in simulation, with (red) and without (blue) the delta-command policy. The black curve represents the torso height variation over time. During data collection, the robot is commanded to move along the x -axis at a velocity of 0.7 m/s.

Here, N_{steps} indicates the maximum number of time steps within a command cycle. p_o^{xy} and p^{xy} represent the robot’s world-frame positions at the beginning and the end of the command cycle, respectively. ε_{lin} , ε_{ang} and ε_{dis} are empirically defined threshold values. Among these metrics, \mathcal{C}_{lin} and \mathcal{C}_{ang} measure the velocity tracking accuracy during a command cycle, \mathcal{C}_{dis} captures the traveled distance, and $\mathcal{C}_{\text{force}}$ reflects whether the sampled force command attains its current upper bound. Once a command cycle is completed, the upper bound of the force is updated as follows:

$$f_{t+1}^{\max} = \begin{cases} \min(f_t^{\max} + \Delta f, f^{\max}), & \text{if } \mathcal{C}, \\ f_t^{\max}, & \text{otherwise,} \end{cases} \quad (13)$$

where f^{\max} denotes the maximum force goal for the curriculum training, and Δf represents the incremental step.

In the lower-body curriculum training, the condition \mathcal{C}_{dis} ensures that the agent prioritizes acquiring basic locomotion skills before gradually learning to exert forces on the environment. The conditions \mathcal{C}_{lin} and \mathcal{C}_{ang} serve as evaluation metrics to ensure that the agent maintains adequate locomotion performance while progressing in force-capable training. Together, these three conditions enforce a staged training process for the lower-body policy. Moreover, the carefully designed force command sampling strategy, as defined in (10), enhances the agent’s generalization ability. The curriculum training progress exhibits a decelerating trend as the f_t^{\max} is progressively increased. In the absence of the sampling strategy, the target force f_t^* may remain consistently high values, causing the agent, after prolonged training under large-force targets, to converge toward a local optimum that only adapts to large forces (as illustrated in Fig. 3). Consequently, the proposed sampling strategy prevents the agent from forgetting previously acquired low-force capabilities, facilitating the acquisition of the force-capable skill.

D. Whole Body Control via Delta-command Policy

The decoupled training of the upper- and lower-body policies provides the robot with effective loco-manipulation capabilities. However, the upper-body policy, which primarily learns end-effector pose tracking in the torso frame, is

TABLE I
OBSERVATIONS AND TRAINING CONFIGURATIONS

Term	Upper-body	Lower-body	Delta-command
Observation	$\mathbf{s}_t^u, \mathcal{G}_t^u$	$\mathbf{s}_t^l, \hat{\mathbf{v}}_t, \mathcal{G}_t^l$	$\mathbf{s}_t, \hat{\mathbf{v}}_t, \hat{\mathbf{x}}_t^{\text{world}}, \mathcal{G}_t^h$
Action scale	0.5	0.1	0.1
Iterations	3000	15000	3000
Parallel envs.	4096		
Actor hidden size	[512, 256, 128]		
Critic hidden size	[512, 256, 128]		
Activation function	ELU		

inevitably influenced by lower-body movements. Moreover, certain loco-manipulation tasks, such as cart-pushing, require the end-effector to maintain a constant height in the world frame. Therefore, the ability to regulate the end-effector pose directly in the world frame becomes indispensable. To address this limitation, a high-level delta-command policy is introduced. In contrast to the basic policy, this policy does not produce independent actions, but rather generates the upper-body policy’s tracking objectives, thereby enabling the robot to acquire end-effector control ability in the world frame.

The core objective of the delta-command agent is to maintain the end-effector’s height and roll-pitch orientation constant in the world frame, thereby mitigating disturbances caused by lower-body motions and other dynamic factors. In contrast, no constraints are imposed on the end-effector’s displacement in the xy -plane or its yaw angle, since enforcing such a restriction in loco-manipulation tasks would almost eliminate the robot’s locomotion capability. Based on this motivation, the delta-command policy is defined as follows:

$$\pi^h : \langle \mathbf{s}_t, \mathbf{a}_{t-1}^h \rangle \times \mathcal{G}_t^h \mapsto \mathbf{a}_t^h \in \mathbb{R}^6. \quad (14)$$

Here, the action \mathbf{a}_t^h represents the goal poses of both left and right end-effectors in terms of z -axis height and roll-pitch orientation, which are relative to world frame. Accordingly, the upper-body goal is obtained by augmenting the baseline command $\mathcal{G}_{\text{ref}}^u \in \mathbb{R}^{12}$ with the delta-command $\mathbf{a}_t^h \in \mathbb{R}^6$:

$$\mathcal{G}_t^u = \mathcal{F}(\mathbf{a}_t^h, \mathcal{G}_{\text{ref}}^u), \quad (15)$$

where $\mathcal{G}_{\text{ref}}^u$ denotes the baseline upper-body goal, and function $\mathcal{F}(\cdot)$ modifies the vector $\mathcal{G}_{\text{ref}}^u$. Specifically, it preserves all entries of $\mathcal{G}_{\text{ref}}^u$ with the exception of the six dimensions associated with the end-effectors’ height and roll-pitch, where it applies an element-wise addition of the vector \mathbf{a}_t^h . Through this modification, the delta-command policy maintains the end-effectors’ height and their roll-pitch orientations in the world frame, while adjustments of $\mathcal{G}_{\text{ref}}^u$ control the xy -axis displacements and yaw rotation relative to the torso frame.

Fig. 4 illustrates the effectiveness of the proposed delta-command policy. The three curves correspond to the torso height (black curve), the end-effector height without the policy (blue curve), and the end-effector height with the policy (red curve) in the world frame. The initial sharp drop is attributed to simulation initialization. During locomotion, the torso exhibits a periodic oscillatory pattern, which directly propagates to the end-effector. Without the delta-command policy, the end-effector follows this oscillation with even greater amplitude.

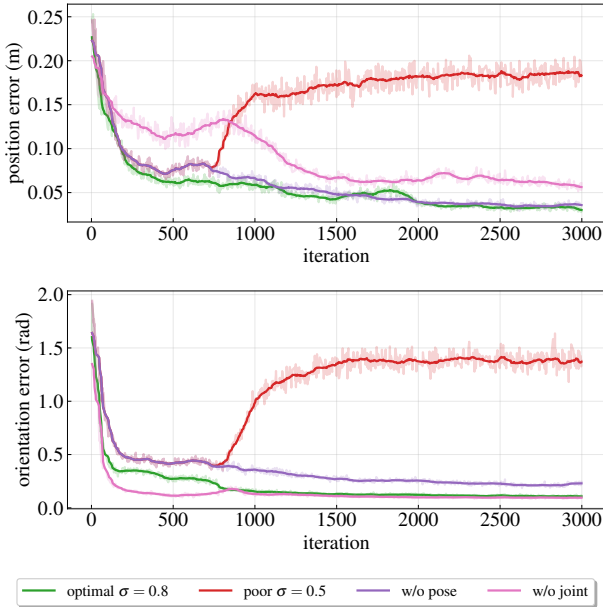


Fig. 5. Position and orientation errors of the left end-effector during training for four ablation groups: optimal σ (heuristic reward with optimal σ), poor σ (heuristic reward with undesirable σ), w/o pose (without task-space term), and w/o joint (without joint-space term).

In contrast, with the delta-command policy, the end-effector is regulated around the target height of 0.9m, effectively mitigating disturbances induced by lower-body motion. After excluding initialization transients, the oscillation amplitude of the end-effector is reduced from 3.5cm (without policy) to 1.5cm (with policy), corresponding to a 57% reduction.

IV. EXPERIMENTS AND RESULTS

This section presents the experimental validation of the proposed whole-body control framework. We evaluate the learned policies across diverse tasks and scenarios to demonstrate their effectiveness and generalization capability. Ablation studies further highlight that the heuristic reward design for upper-body control, and the curriculum learning strategy for lower-body training significantly accelerate and stabilize policy optimization. Finally, hardware experiments validate that our method successfully bridges the sim-to-real gap and achieves compelling performance in actual environments.

A. Training

We employ IsaacSim as the simulation environment for both training and evaluation of the humanoid robot. The training is conducted on a computing platform equipped with a AMD 7950X CPU and an NVIDIA RTX 4090D GPU.

The off-the-shelf RL algorithm, PPO [43], is adopted for policy optimization. Since the states of the physical robot are only partially observable in real-world, the asymmetric actor-critic network is adopted during the training of the lower-body and delta-command agents. The corresponding observations and the training configurations are summarized in Table I, where (°) indicates privileged information accessible only to the critics during training but not during deployment.

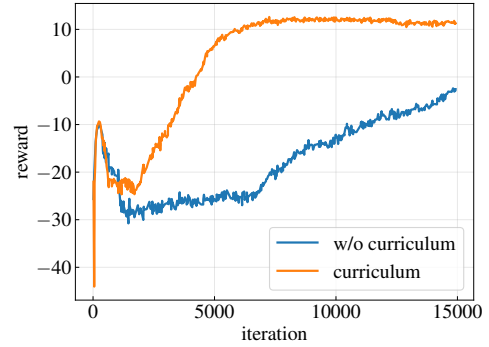


Fig. 6. Comparison of curriculum reward evolution between agents trained with and w/o curriculum learning.

Regarding the goal space, the upper-body targets are computed through forward kinematics following Alg. 1. The orientation aperture δ in task-space is set to π . For the lower body, the target linear velocity along the x -axis is sampled as $v_x^* \sim \mathcal{U}(-0.6, 1.0)$ m/s, the target angular velocity around the z -axis as $\omega_z^* \sim \mathcal{U}(-\frac{\pi}{2}, \frac{\pi}{2})$ rad, and the maximum force goal $f^{\max} = 50$ N. The target space of the delta-command is defined as $\mathbf{d}_z^{\text{world}*} \sim \mathcal{U}(0.85, 1)$ m, $\psi_r^{\text{world}*} \sim \mathcal{U}(-\frac{\pi}{2}, \frac{\pi}{2})$ rad, and $\psi_p^{\text{world}*} \sim \mathcal{U}(-\frac{\pi}{2}, \frac{\pi}{2})$ rad, which aims to maintain the end-effector’s vertical displacement $\mathbf{d}_z^{\text{world}*}$ in world frame, together with the desired roll and pitch rotations, denoted as $\psi_r^{\text{world}*}$ and $\psi_p^{\text{world}*}$, respectively.

To encourage effective exploration, all three agents are trained with purely regularization-based reward functions, as detailed in Table II. Here, the symbol “1” denotes the indicator function, \mathbf{q}_{rpy}^i are the roll-pitch-yaw rotational joints of body link i , T_{air} is the single-foot air time at target speed exceeds 0.1 m/s, $\mathbf{F}_j^{\text{feet}}$ represents force on feet along direction j , while “ \rightarrow ” indicates that the corresponding weight varies over the course of training.

Moreover, to bridge the gap between simulation and real-world, the domain randomization terms listed in Table III are incorporated during the training process. To ensure that the robot can successfully exert force on the external environment, an additional force application term at the end-effectors of upper-body is introduced.

During the training of upper-body, the robot’s torso link is fixed in the simulation environment, such that only the motions of the upper-body joints are considered. Besides, the training of the upper-body policy is conducted in stages. A sliding window of 100 episodes is employed, and if the reward values within the window vary by less than 1.5, the policy is considered to be approaching convergence, at which point the parameters α^{pose} and σ are automatically adjusted and the training proceeds to the next stage. Reducing σ or increasing α^{joint} both amplify the sensitivity of the reward to joint errors. However, owing to the exponential-form term, adjusting σ provides a more efficient way to modulate this sensitivity. Consequently, α^{joint} is kept constant at 1, and only σ is varied.

In lower-body training, the thresholds are set as $\varepsilon_{\text{jin}} = 0.3$, $\varepsilon_{\text{ang}} = 0.45$, $\varepsilon_{\text{dis}} = 4$. Since domain randomization terms such as push robot are introduced, the tracking metrics for linear and angular velocity should not be designed overly strict. And

TABLE II
REWARD TERMS AND WEIGHTS

Reward Term	Function	Weights		
		Upper-body	Lower-body	Delta-command
Linear velocity tracking (root)	$\exp(-\ \mathbf{v}_{xy}^* - \mathbf{v}_{xy}\ _2^2/0.5^2)$	-	1	-
Linear velocity penalty (root)	v_z^2	-	-1	-
Angular velocity tracking (root)	$\exp(-\ \omega_z^* - \omega_z\ _2^2/0.5^2)$	-	1	-
Angular velocity penalty (root)	$-\ \omega_{xy}\ _2^2$	-	-0.05	-
Angle velocity penalty (head)	$-\ \omega_{xy}^{\text{head}}\ _2^2$	-	-0.5	-
Termination penalty	$\mathbf{1}[\text{termination}]$	-	-200	-200
Joint acceleration penalty	$\ \ddot{\mathbf{q}}\ _2^2$	-	-2.5e-7	-
Joint torque penalty	$\sum_i \boldsymbol{\tau}_i \cdot \dot{\mathbf{q}}_i $	-	-1e-3	-
Joint position limits	$\sum_i \max(\mathbf{q}_i - 0.9 \cdot \mathbf{q}_{\text{lim},i}, 0)$	-	-2.0	-
Collision penalty	$\mathbf{1}[\text{collision}]$	-1	-1	-1
Straight body	$\ \mathbf{g}_{xy}\ _2^2$	-	-1	-
Feet air time [42]	$0.3 \cdot \min(T_{\text{air}}, 0.4)$	-	0.15	-
Feet slide	$\sum_i \mathbf{1}[\text{contact}_i] \cdot \ \mathbf{v}_{xy,i}^{\text{feet}}\ _2$	-	-0.25	-
Feet stumble	$\mathbf{1}[\ \mathbf{F}_{xy}^{\text{feet}}\ > 5 F_z^{\text{feet}}]$	-	-2.0	-
Feet force	$\min(\max(F_z^{\text{feet}} - 500, 0), 400)$	-	-3e-3	-
Joint deviation (waist)	$\sum \mathbf{q}_{rp}^{\text{waist}} - \mathbf{q}^{\text{default}} $	-	-1.2	-
Joint deviation (hip)	$\sum \mathbf{q}_{rp}^{\text{hip}} - \mathbf{q}^{\text{default}} $	-	-0.15	-
Joint deviation (knee)	$\sum \mathbf{q}_p^{\text{knee}} - \mathbf{q}^{\text{default}} $	-	-0.02	-
Joint deviation (ankle)	$\sum \mathbf{q}_{rp}^{\text{ankle}} - \mathbf{q}^{\text{default}} $	-	-0.02	-
Action rate	$\ \mathbf{a}_t - \mathbf{a}_{t-1}\ _2^2$	-1e-4 \rightarrow -0.1	-0.01	-0.5
Heuristic reward	(7)	1	-	-
Joint velocity	$\ \dot{\mathbf{q}}\ _2^2$	-1e-4 \rightarrow -2e-3	-	-
Action	$\ \mathbf{a}_t\ _2^2$	-	-	-0.02
End-effector height	$\ \mathbf{d}_z^{\text{world}*} - \mathbf{d}_z^{\text{world}}\ _2^2$	-	-	-10
End-effector orientation	$\sum_i \ \text{Log}(\eta_i^{\text{world}} \otimes \eta_i^{\text{world}*})\ $	-	-	-6

TABLE III
DOMAIN RANDOMIZATION TERMS

Term	Specification	Upper-body	Lower-body	Delta-command
Static friction	$\mathcal{U}(0.6, 1.0)$	✓	✓	✓
Dynamic friction	$\mathcal{U}(0.4, 0.8)$	✓	✓	✓
Torso link mass	$\mathcal{U}(-5, 5) + \text{default kg}$	-	✓	✓
Hand link mass	$\mathcal{U}(1.0, 1.5) \times \text{default kg}$	✓	✓	✓
Root velocity	$\mathcal{U}(-0.5, 0.5) \text{ m/s}$	-	✓	✓
Joint position	$\mathcal{U}(0.5, 1.5) \times \mathbf{q}^{\text{default}} \text{ rad}$	✓	✓	✓
Push robot	interval $\in [10, 15] \text{ s}$, $\mathbf{v}_{xy} \in [-1, 1] \text{ m/s}$	-	✓	✓
Add force on hand	interval $\in [2, 5] \text{ s}$, $F \in [0, 35] \text{ N}$	✓	✓	✓

TABLE IV
UPPER-BODY ABLATION GROUPS AND RESULTS

Training	α^{joint}		α^{pose}			σ			Position error ↓	Orientation error ↓
	Stage I	Stage I	Stage II	Stage III	Stage I	Stage II	Stage III			
Optimal σ	1	0	-0.2	-2	2	1	0.8	0.03	0.11	
Poor σ	1	0	-0.2	-2	2	0.5	-	0.17	1.32	
w/o pose	1	0	-	-	2	1	0.8	0.04	0.21	
w/o joint	0	-0.2	-2	0	-	-	-	0.05	0.11	

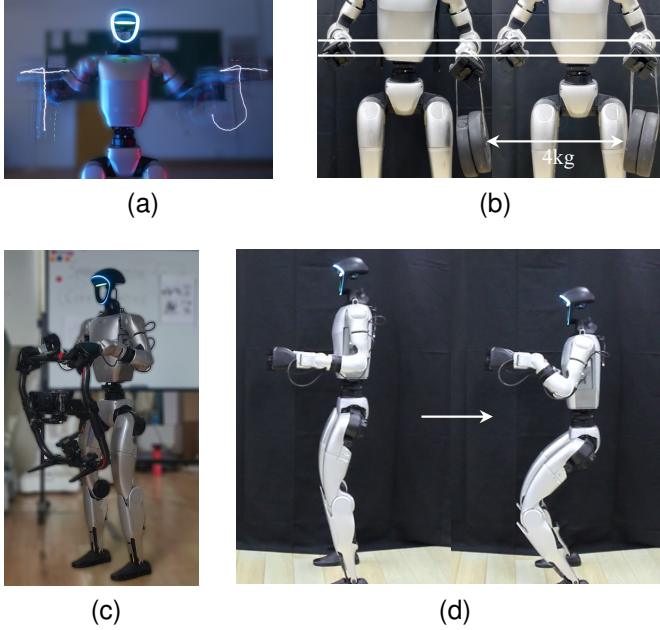


Fig. 7. Hardware experiment details. (a) The end-effector trajectories showed by LED light. (b) End-effector poses under a 4 kg payload. Without the delta-command policy (left), a clear downward displacement occurs, while with the policy (right), the end-effector is maintained closer to the desired pose. (c) The robot holds a gimbal. (d) The delta-command policy maintains the end-effector poses constant in the world frame while the robot squats.

the update step size Δf is set to 2 N. Meanwhile, the upper-body policy runs inference in the lower-body training process, enabling the policy to generalize to disturbances caused by the upper-body movements.

B. Ablation Studies

Ablation studies are conducted to systematically assess the contribution of each key component within the proposed training pipeline.

Upper-body training pipeline. Comparative experiments are conducted to evaluate the impact of the heuristic reward function. Based on different σ update steps and module ablations, four ablation groups is defined, summarized in Table IV, where Stage I denotes the initial values. Fig. 5 visualizes the position and orientation errors of the left end-effector during training for all four groups.

The results show that combining both joint- and task-space terms achieves the best performance. However, the “poor σ ” group indicates that excessively large σ update steps cause the heuristic reward to drop sharply, resulting in the agent focusing more on other reward terms, which in turn leads to an increase in both position and orientation errors. The “w/o pose” group shows that tracking only joint angles can still achieve reasonable position accuracy, but small angle errors in proximal joints propagate along the kinematic chain and degrade orientation tracking. In contrast, the “w/o joint” group reduces orientation error quickly, but without guidance from forward kinematics, the position error decreases slowly. Overall, these ablation results demonstrate the effectiveness

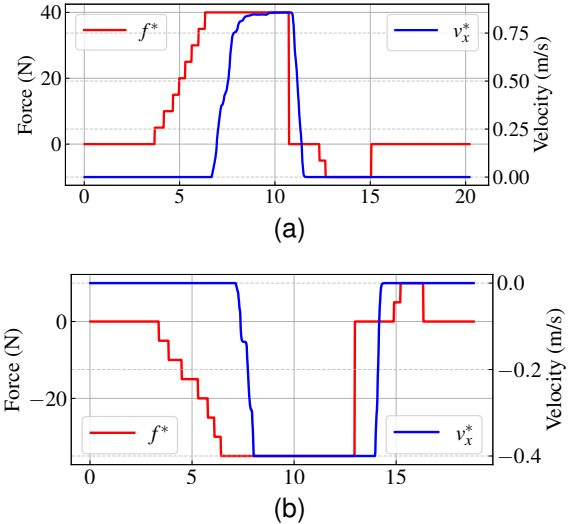


Fig. 8. Time series of control signals in the cart-manipulation experiments. (a) Cart-pushing task. (b) Cart-pulling task.

of the heuristic reward, enabling faster policy convergence to higher upper-body performance.

Lower-body training pipeline. Lower-body ablation is performed to evaluate the impact of curriculum learning. In the absence of curriculum training, the agent samples force targets at the beginning of training as $f_t^* \sim \mathcal{U}(0, f^{\max})$. In contrast, under curriculum training, force updates are restricted until (11) is satisfied.

The evolution of curriculum reward with and without curriculum learning is depicted in Fig. 6. The evolution indicate that, with curriculum learning, the policy converges as early as iteration 8000, whereas without curriculum learning, no convergence is observed within the entire training horizon. These findings suggest that curriculum learning substantially accelerates the convergence process during training. The underlying reason is that, without curriculum learning, the agent is required to track force targets before acquiring the fundamental locomotion skills, and the premature emphasis on force-capable skill severely impedes the learning of locomotion. By contrast, curriculum learning enables a progressive acquisition of skills from simple to complex, which proves to be highly effective. Furthermore, the efficacy of the sampling strategy within the curriculum learning framework has been previously validated, as illustrated in Fig. 3.

C. Real-world Experiments

To further validate the effectiveness of the proposed approach, particularly its sim-to-real transferability and real-world deployment performance, hardware experiments are conducted on the Unitree G1 robot, which is equipped with two Dex3-1 dexterous hands at the upper-body end-effectors. In the real-world deployment, the robot operates at a control frequency of 50 Hz, concurrently executing all three policies on the onboard Jetson Orin NX without additional fine-tuning. The policies are deployed in Just-In-Time (JIT) mode, with inference implemented in C++ via the ONNX Runtime to achieve real-time performance.

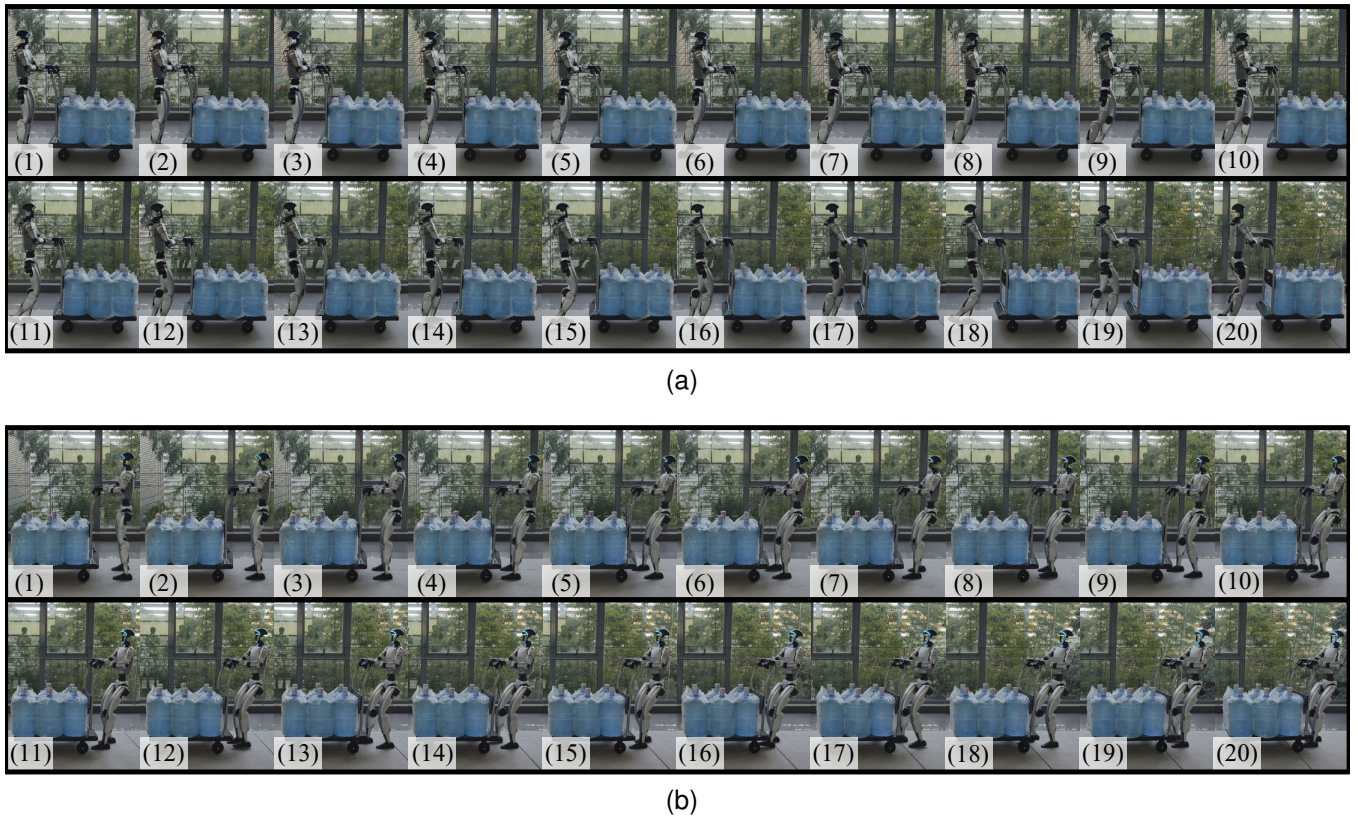


Fig. 9. Snapshots of the cart-manipulation experiments. (a) Cart-pushing task. (b) Cart-pulling task.

A visualization of selected hardware experiment details is presented in Fig. 7. Here, Fig. 7(a) illustrates the upper-body policy’s pose tracking capabilities. To visualize the end-effectors’ trajectories, LED beads are affixed to both end-effectors, and their trajectory is recorded via long-exposure photography. Specifically, the robot’s left hand is commanded to track a trajectory in the shape of the letter “T”, while the right hand is commanded to track a trajectory in the shape of the letter “J”. Both target letters are designed to be 20 cm high and 10 cm wide. The clear resulting trajectories from the LED beads provide qualitative evidence of the upper-body policy’s tracking performance. Fig. 7(b) illustrates that the delta-command policy effectively mitigates the end-effector pose deviation caused by upper-body payloads. The robot end-effector is initialized to the same pose in both cases, with and without the delta-command policy, after which a 4 kg payload is attached to the end-effector. A clear difference in end-effector height is observed, which demonstrates that the delta-command policy enhances end-effector control in loco-manipulation tasks. Fig. 7(c) shows the robot holding a 3.9 kg camera gimbal while maintaining standing. This experiment demonstrates that the upper-body policy, after domain randomization, acquires the ability to accommodate payloads. Meanwhile, the lower-body policy generalizes to the additional upper-body load and preserves stable locomotion performance. Besides, Fig. 7(d) demonstrates the capability of the delta-command policy to maintain the end-effector pose in the world frame. The desired height of the end-effector is 0.9 m in world frame, while its target roll and pitch orientation

is zero. When the robot is commanded to squat by 10 cm, the end-effector pose remains constant, effectively compensating for the downward displacement caused by knee flexion.

Finally, to evaluate the collaborative performance of the three policies in loco-manipulation tasks, a cart-manipulation experiment reflecting an industrial scenario is conducted. The pushing and pulling time-varying control signals are depicted in Fig. 8 and the snapshots of the robot action are shown in Fig. 9. The experiment is set up on a moderately frictional plaster floor, with a payload of six water buckets (18.8 kg each, totaling 112.8 kg) placed on the cart. The horizontal bar of the cart is 0.9 m above the ground and serves as d_z^{world} for the delta-command policy. Control signals are composed of continuous velocity commands, while the force commands are discretized and modified in 5 N steps or reset to zero.

Cart-pushing. As shown in Fig. 8(a) and Fig. 9(a), the robot remains stationary without receiving control commands during 0 to 3.7 s. From 3.7 to 6.3 s, the force command increases from 0 to 40 N, during which the lower-body policy leverages its force-capable skill to actively apply force to the cart. This process corresponds to snapshots (1)–(7) in Fig. 9(a), as the robot exhibits a noticeable forward lean without displacement. Once the cart begins to move, the velocity command is increased to 0.8 m/s, prompting the robot to advance. During the stopping phase, the force and velocity commands are sequentially reduced to zero, after which the robot briefly applies a reverse force to counteract the cart’s momentum.

Cart-pulling. The experiment details are shown in Fig. 8(b) and Fig. 9(b). During 3.4 to 6.4 s, the robot applies a pulling

force of 35 N through the force-capable skill. This process corresponds to snapshots (1)–(4) in Fig. 9(b), where the robot exhibits a marked backward lean. Following the onset of cart motion, the velocity command varies to -0.4 m/s, and the robot engages in pulling. During stopping, the robot similarly applies a brief counterforce to assist the cart to rest. In addition, an interesting phenomenon in the experiments is observed. In the cart-pushing task, the forward-leaning posture that emerges when applying force (snapshot (7) in Fig. 9(a)) is not preserved during the subsequent movement (snapshots (12)–(20) in Fig. 9(a)). In contrast, in the cart-pulling task, the backward-leaning posture established during force exertion (snapshot (4) in Fig. 9(b)) is maintained throughout the following motion (snapshots (5)–(20) in Fig. 9(b)). This backward inclination enables the robot to pull the cart with a smaller active force compared to pushing.

Overall, the coordinated operation of the three policies enables the robot to perform high-payload cart-manipulation tasks, demonstrating the effectiveness of the proposed approach in loco-manipulation and its potential for industrial applications.

V. CONCLUSION

This paper presents a multi-policy framework based on RL to tackle humanoid loco-manipulation tasks in high-load industrial scenarios. The proposed framework consists of three distinct policies: an upper-body policy, a lower-body policy, and a delta-command policy. For the upper-body policy, a heuristic reward function is introduced to guide the policy with forward kinematics priors. This reward significantly accelerates policy convergence and improves end-effector tracking performance. The lower-body policy is endowed with the capability of actively exerting forces on the environment. A curriculum learning scheme is meticulously designed for this policy, which ensures a sequential acquisition of skills and substantially improves training efficiency. Meanwhile, the delta-command policy, rather than directly controlling the robot, generates the tracking targets of the upper-body policy to achieve end-effector pose tracking in world-frame.

We conduct extensive evaluations in both simulation and real-world settings to examine the proposed approach. Notably, in the cart-manipulation task, the coordinated integration of the three policies enabled the G1 humanoid robot to push and pull a cart with a payload of 112.8 kg, demonstrating the framework’s strong potential for industrial applications.

Future work will focus on expanding the robot’s force control capabilities, as the current framework is limited to applying forces in a forward or backward direction.

REFERENCES

- [1] Z. Fu, Q. Zhao, Q. Wu, G. Wetzstein, and C. Finn, “Humanplus: Humanoid shadowing and imitation from humans,” in *Conference on Robot Learning*. PMLR, 2025, pp. 2828–2844.
- [2] Q. Ben, F. Jia, J. Zeng, J. Dong, D. Lin, and J. Pang, “Homie: Humanoid loco-manipulation with isomorphic exoskeleton cockpit,” in *RSS 2025 Workshop on Whole-body Control and Bimanual Manipulation: Applications in Humanoids and Beyond*.
- [3] J. Kim, A. K. Mishra, R. Limosani, M. Scaforo, N. Cauli, J. Santos-Victor, B. Mazzolai, and F. Cavallo, “Control strategies for cleaning robots in domestic applications: A comprehensive review,” *International Journal of Advanced Robotic Systems*, vol. 16, no. 4, p. 1729881419857432, 2019.
- [4] S. Saeedvand, H. Mandala, and J. Baltes, “Hierarchical deep reinforcement learning to drag heavy objects by adult-sized humanoid robot,” *Applied Soft Computing*, vol. 110, p. 107601, 2021.
- [5] H. Song, W. Z. Peng, and J. H. Kim, “Effects of object mass on balancing for whole-body lifting tasks,” in *2023 IEEE-RAS 22nd International Conference on Humanoid Robots (Humanoids)*, 2023, pp. 1–8.
- [6] J. C. Vaz and P. Oh, “Material handling by humanoid robot while pushing carts using a walking pattern based on capture point,” in *2020 IEEE International Conference on Robotics and Automation (ICRA)*, 2020, pp. 9796–9801.
- [7] J. He, C. Zhang, F. Jenelten, R. Grandia, M. Bächer, and M. Hutter, “Attention-based map encoding for learning generalized legged locomotion,” *Science Robotics*, vol. 10, no. 105, p. eadv3604, 2025.
- [8] T. He, J. Gao, W. Xiao, Y. Zhang, Z. Wang, J. Wang, Z. Luo, G. He, N. Sobanbab, C. Pan *et al.*, “Asap: Aligning simulation and real-world physics for learning agile humanoid whole-body skills,” *arXiv preprint arXiv:2502.01143*, 2025.
- [9] J. Li, X. Cheng, T. Huang, S. Yang, R.-Z. Qiu, and X. Wang, “Amo: Adaptive motion optimization for hyper-dexterous humanoid whole-body control,” *arXiv preprint arXiv:2505.03738*, 2025.
- [10] X. Cheng, Y. Ji, J. Chen, R. Yang, G. Yang, and X. Wang, “Expressive whole-body control for humanoid robots,” *arXiv preprint arXiv:2402.16796*, 2024.
- [11] Y. Zhang, Y. Yuan, P. Gurunath, T. He, S. Omidshafiei, A.-a. Aghamohammadi, M. Vazquez-Chanlatte, L. Pedersen, and G. Shi, “Falcon: Learning force-adaptive humanoid loco-manipulation,” *arXiv e-prints*, pp. arXiv–2505, 2025.
- [12] C. Lu, X. Cheng, J. Li, S. Yang, M. Ji, C. Yuan, G. Yang, S. Yi, and X. Wang, “Mobile-television: Predictive motion priors for humanoid whole-body control,” *arXiv preprint arXiv:2412.07773*, 2024.
- [13] T. He, Z. Luo, W. Xiao, C. Zhang, K. Kitani, C. Liu, and G. Shi, “Learning human-to-humanoid real-time whole-body teleoperation,” in *2024 IEEE/RSJ International Conference on Intelligent Robots and Systems (IROS)*. IEEE, 2024, pp. 8944–8951.
- [14] M. Ji, X. Peng, F. Liu, J. Li, G. Yang, X. Cheng, and X. Wang, “Exbody2: Advanced expressive humanoid whole-body control,” in *RSS 2025 Workshop on Whole-body Control and Bimanual Manipulation: Applications in Humanoids and Beyond*.
- [15] T. Zhang, B. Zheng, R. Nai, Y. Hu, Y.-J. Wang, G. Chen, F. Lin, J. Li, C. Hong, K. Sreenath *et al.*, “Hub: Learning extreme humanoid balance,” in *RSS 2025 Workshop on Whole-body Control and Bimanual Manipulation: Applications in Humanoids and Beyond*.
- [16] X. Tian, Q. Xu, and Q. Zhan, “An analytical inverse kinematics solution with joint limits avoidance of 7-dof anthropomorphic manipulators without offset,” *Journal of the Franklin Institute*, vol. 358, no. 2, pp. 1252–1272, 2021.
- [17] Z. Ding, H. Jiang, Y. Wang, Z. Sun, Y. Zhang, X. Niu, M. Yang, W. Zeng, X. Xu, and Z. Lu, “Jaeger: Dual-level humanoid whole-body controller,” *arXiv preprint arXiv:2505.06584*, 2025.
- [18] P. M. Wensing, M. Posa, Y. Hu, A. Escande, N. Mansard, and A. Del Prete, “Optimization-based control for dynamic legged robots,” *IEEE Transactions on Robotics*, vol. 40, pp. 43–63, 2023.
- [19] J. Li and Q. Nguyen, “Kinodynamic pose optimization for humanoid loco-manipulation,” in *2023 IEEE-RAS 22nd International Conference on Humanoid Robots (Humanoids)*, 2023, pp. 1–8.
- [20] M. Sombolstan and Q. Nguyen, “Hierarchical adaptive loco-manipulation control for quadruped robots,” in *2023 IEEE International Conference on Robotics and Automation (ICRA)*, 2023, pp. 12156–12162.
- [21] K. Bouyarmane, K. Chappellet, J. Vaillant, and A. Kheddar, “Quadratic programming for multirobot and task-space force control,” *IEEE Transactions on Robotics*, vol. 35, no. 1, pp. 64–77, 2018.
- [22] M. Murooka, K. Chappellet, A. Tanguy, M. Benallegue, I. Kumagai, M. Morisawa, F. Kanehiro, and A. Kheddar, “Humanoid loco-manipulations pattern generation and stabilization control,” *IEEE Robotics and Automation Letters*, vol. 6, no. 3, pp. 5597–5604, 2021.
- [23] J. Li, J. Ma, O. Kolt, M. Shah, and Q. Nguyen, “Dynamic loco-manipulation on hector: Humanoid for enhanced control and open-source research,” *arXiv preprint arXiv:2312.11868*, 2023.
- [24] A. Rioux and W. Suleiman, “Humanoid navigation and heavy load transportation in a cluttered environment,” in *2015 IEEE/RSJ International*

- Conference on Intelligent Robots and Systems (IROS)*. IEEE, 2015, pp. 2180–2186.
- [25] S. Nozawa, I. Kumagai, Y. Kakiuchi, K. Okada, and M. Inaba, “Humanoid full-body controller adapting constraints in structured objects through updating task-level reference force,” in *2012 IEEE/RSJ International Conference on Intelligent Robots and Systems*, 2012, pp. 3417–3424.
- [26] J. Lee, J. Hwangbo, L. Wellhausen, V. Koltun, and M. Hutter, “Learning quadrupedal locomotion over challenging terrain,” *Science robotics*, vol. 5, no. 47, p. eabc5986, 2020.
- [27] J. Tan, T. Zhang, E. Coumans, A. Iscen, Y. Bai, D. Hafner, S. Bohez, and V. Vanhoucke, “Sim-to-real: Learning agile locomotion for quadruped robots,” *arXiv preprint arXiv:1804.10332*, 2018.
- [28] I. Radosavovic, T. Xiao, B. Zhang, T. Darrell, J. Malik, and K. Sreenath, “Real-world humanoid locomotion with reinforcement learning,” *Science Robotics*, vol. 9, no. 89, p. eadi9579, 2024.
- [29] M. Mittal, C. Yu, Q. Yu, J. Liu, N. Rudin, D. Hoeller, J. L. Yuan, R. Singh, Y. Guo, H. Mazhar, A. Mandlekar, B. Babich, G. State, M. Hutter, and A. Garg, “Orbit: A unified simulation framework for interactive robot learning environments,” *IEEE Robotics and Automation Letters*, vol. 8, no. 6, pp. 3740–3747, 2023.
- [30] K. Zakka, B. Tabanpour, Q. Liao, M. Haiderbhai, S. Holt, J. Y. Luo, A. Allshire, E. Frey, K. Sreenath, L. A. Kahrs *et al.*, “Mujoco playground,” *CoRR*, 2025.
- [31] Z. Li, X. B. Peng, P. Abbeel, S. Levine, G. Berseth, and K. Sreenath, “Robust and versatile bipedal jumping control through reinforcement learning,” in *Robotics science and systems*. RSS, 2023.
- [32] W. Sun, B. Cao, L. Chen, Y. Su, Y. Liu, Z. Xie, and H. Liu, “Learning perceptive humanoid locomotion over challenging terrain,” *arXiv preprint arXiv:2503.00692*, 2025.
- [33] Z. Zhuang, S. Yao, and H. Zhao, “Humanoid parkour learning,” *arXiv preprint arXiv:2406.10759*, 2024.
- [34] J. Dao, H. Duan, and A. Fern, “Sim-to-real learning for humanoid box loco-manipulation,” in *2024 IEEE International Conference on Robotics and Automation (ICRA)*. IEEE, 2024, pp. 16930–16936.
- [35] Z. Li, X. Cheng, X. B. Peng, P. Abbeel, S. Levine, G. Berseth, and K. Sreenath, “Reinforcement learning for robust parameterized locomotion control of bipedal robots,” in *2021 IEEE International Conference on Robotics and Automation (ICRA)*. IEEE, 2021, pp. 2811–2817.
- [36] M. Seo, S. Han, K. Sim, S. H. Bang, C. Gonzalez, L. Sentis, and Y. Zhu, “Deep imitation learning for humanoid loco-manipulation through human teleoperation,” in *2023 IEEE-RAS 22nd International Conference on Humanoid Robots (Humanoids)*, 2023, pp. 1–8.
- [37] C. Zhang, W. Xiao, T. He, and G. Shi, “Wococo: Learning whole-body humanoid control with sequential contacts,” in *Conference on Robot Learning*. PMLR, 2025, pp. 455–472.
- [38] X. B. Peng, Z. Ma, P. Abbeel, S. Levine, and A. Kanazawa, “Amp: Adversarial motion priors for stylized physics-based character control,” *ACM Transactions on Graphics (ToG)*, vol. 40, no. 4, pp. 1–20, 2021.
- [39] Y. Ze, Z. Chen, J. P. Araújo, Z. ang Cao, X. B. Peng, J. Wu, and C. K. Liu, “Twist: Teleoperated whole-body imitation system,” 2025. [Online]. Available: <https://arxiv.org/abs/2505.02833>
- [40] Z. Xu, M. Hu, K. Xiao, Q. Fang, C. Liu, and Q. Chen, “Realizing text-driven motion generation on nao robot: A reinforcement learning-optimized control pipeline,” *arXiv preprint arXiv:2506.05117*, 2025.
- [41] W. Xie, J. Han, J. Zheng, H. Li, X. Liu, J. Shi, W. Zhang, C. Bai, and X. Li, “Kungfubot: Physics-based humanoid whole-body control for learning highly-dynamic skills,” *arXiv preprint arXiv:2506.12851*, 2025.
- [42] N. Rudin, D. Hoeller, P. Reist, and M. Hutter, “Learning to walk in minutes using massively parallel deep reinforcement learning,” in *Proceedings of the 5th Conference on Robot Learning*, ser. Proceedings of Machine Learning Research, vol. 164. PMLR, 2022, pp. 91–100. [Online]. Available: <https://proceedings.mlr.press/v164/rudin22a.html>
- [43] J. Schulman, F. Wolski, P. Dhariwal, A. Radford, and O. Klimov, “Proximal policy optimization algorithms,” *arXiv preprint arXiv:1707.06347*, 2017.